

An advanced electric propulsion diagnostic (AEPD) platform for in-situ characterization of electric propulsion thrusters and ion beam sources^{*}

Carsten Bundesmann^{1,a}, Christoph Eichhorn¹, Frank Scholze¹, Daniel Spemann¹, Horst Neumann¹, Damiano Pagano², Simone Scaranzin², Fabrizio Scortecci², Hans J. Leiter³, Sven Gauter⁴, Ruben Wiese⁴, Holger Kersten⁴, Kristof Holste⁵, Peter Köhler⁵, Peter J. Klar⁵, Stéphane Mazouffre⁶, Richard Blott⁷, Alexandra Bulit⁸, and Käthe Dannenmayer⁸

¹ Leibniz-Institute of Surface Modification, Permoserstr. 15, 04318 Leipzig, Germany

² Aerospazio Tecnologie s.r.l., Via Provinciale Nord 42a, 53040 Rapolano Terme, Siena, Italy

³ Airbus Defence & Space GmbH, Im Langen Grund, 74239 Hardthausen-Lampoldshausen, Germany

⁴ Christian-Albrechts-Universität zu Kiel, Leibnizstr. 11-19, 24098 Kiel, Germany

⁵ Justus-Liebig-Universität Gießen, Heinrich-Buff-Ring 16, 35392 Gießen, Germany

⁶ ICARE, CNRS, 1C Av. de la Recherche Scientifique, 45071 Orléans, France

⁷ Space Enterprise Partnerships Ltd., Bennetts, Eastergate Lane, Chichester, West Sussex PO20 3SJ, UK

⁸ ESA/ESTEC, Keplerlaan 1, 2201 AZ Noordwijk, The Netherlands

Received 4 April 2016

Published online 18 October 2016 – © EDP Sciences, Società Italiana di Fisica, Springer-Verlag 2016

Abstract. Experimental characterization is an essential task in development, qualification and optimization process of electric propulsion thrusters or ion beam sources for material processing, because it can verify that the thruster or ion beam source fulfills the requested mission or application requirements, and it can provide parameters for thruster and plasma modeling. Moreover, there is a need for standardizing electric propulsion thruster diagnostics in order to make characterization results of different thrusters and also from measurements performed in different vacuum facilities reliable and comparable. Therefore, we have developed an advanced electric propulsion diagnostic (AEPD) platform, which allows a comprehensive in-situ characterization of electric propulsion thrusters (or ion beam sources) and could serve as a standard on-ground tool in the future. The AEPD platform uses a five-axis positioning system and provides the option to use diagnostic tools for beam characterization (Faraday probe, retarding potential analyzer, ExB probe, active thermal probe), for optical inspection (telemicroscope, triangular laser head), and for thermal characterization (pyrometer, thermocamera). Here we describe the capabilities of the diagnostic platform and provide first experimental results of the characterization of a gridded ion thruster RIT- μ X.

1 Introduction

Experimental characterization of electric propulsion (EP) thrusters or ion beam sources for material processing may provide important data both to judge their performance and to achieve a better understanding of physical processes in the plume and in the discharge chamber of such systems. Measurements of plasma parameters and monitoring of possible lifetime limiting alteration of the properties of thruster components, such as, for example, the evolution of the grid hole diameter in gridded ion thrusters, yield valuable information for the development and validation of numerical tools. Those codes, e.g. aiming at plasma and ion beam modeling (examples: particle-in-cell

code XOOPIC for charged particle and plasma simulation [1], IGUN code for simulation of ion trajectories [2]) or thruster lifetime prediction related to the erosion of ion thruster accelerator grids (example: DynaSim code [3]), can help to partially circumvent expensive measurement campaigns with respect to thruster design and performance verification.

In this context, several groups have investigated surfaces of thruster components e.g. by telemicroscopy or thermal imaging methods [4–11]. In order to allow for the in-situ measurement of an extensive set of EP thruster performance parameters, the advanced electric propulsion diagnostic (AEPD) platform was designed and built some years ago [12,13]. The setup was modular and mobile such that it could be easily adapted to vacuum facilities of different size and experimental needs. Several measurement devices for particle beam and mechanical part characterization were implemented: a Faraday probe for thruster

^{*} Contribution to the Topical Issue “Physics of Ion Beam Sources”, edited by Holger Kersten and Horst Neumann.

^a e-mail: Carsten.Bundesmann@iom-leipzig.de

plume characterization, an energy-selective mass spectrometer to collect energy distribution data, a telemicroscope to measure erosion of mechanical parts, a triangular laser head to monitor the surface profile of selected parts of interest, and a pyrometer to measure surface temperature distributions. Most of the sensors consisted of commercially available devices with in-house modifications. Only the Faraday probe was manufactured completely in-house. The AEPD platform was tested successfully with two electric propulsion thrusters: a gridded ion thruster RIT-22 (Airbus Defence & Space, Germany [7,10,12]) and a Hall effect thruster SPT-100D EM1 (EDB Fakel, Russia [8,12]), in two different vacuum facilities.

The previous results demonstrated the capabilities of the first AEPD platform but also some limitations, mainly related to the design but also to financial needs. Therefore, a new activity has been started in order to improve the performance and availability of the diagnostic platform. At present, the activities concentrate on three major topics: (i) the setup and test of additional or alternative plasma-diagnostic tools as extension or redesign of AEPD capabilities, (ii) the implementation of partially new designs of existing sensors in order to reduce the dimension and, hence, the interaction of the diagnostic head and thruster, (iii) qualification of the diagnostic platform as standard on-ground tool for EP thruster characterization.

The first aspect deals with the development and integration of new sensors in the AEPD platform, such as a retarding potential analyzer, an ExB probe or an active thermal probe [13]. The second aspect concerns rather technical issues, such as modifications related to the vacuum compatibility of some diagnostic heads, size reduction and optimization of the respective sensor housings and working distance geometries, but also the protection of the sensor heads from damage due to ion bombardment [14]. The third aspect is not addressed in this paper but will be the focus of future work, because standardization of EP diagnostics is key issue when promoting EP technologies.

In this paper, the most recent implementation of the diagnostic tools is described and first performance characterization results are presented, exemplary, for a gridded ion thruster RIT- μ X (Airbus Defence & Space [15]).

2 Experimental setup

2.1 Positioning system

The AEPD platform (see Fig. 1) consists of a 5-axis positioning system and several diagnostic tools. The positioning system utilizes a modular heavy bar setup, on which three ultra-high-vacuum-specified (UHV-specified) linear tables with a traveling range of 700 mm and a traveling speed of typically 30 mm/s, and two UHV-specified rotary tables are mounted. The positioning system can be easily adapted to chambers of different size. Using the linear and rotary tables, the thruster and the diagnostic heads can be positioned very precisely relative to each other, and even 1- and 2-dimensional mappings or angular-dependent

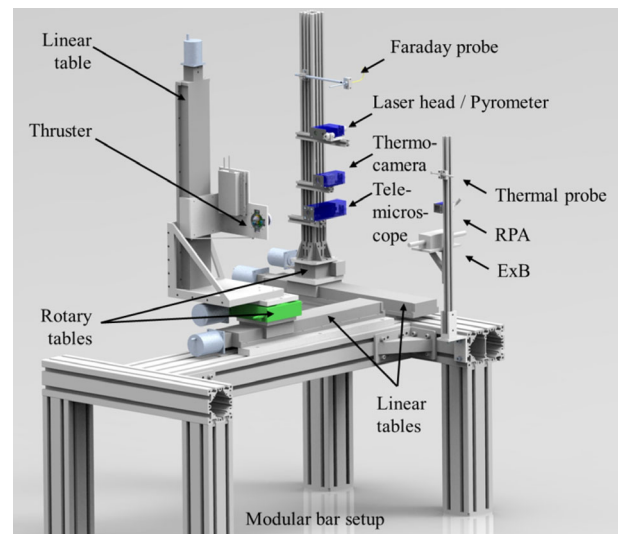


Fig. 1. Drawing of the AEPD platform with modular bar frame, linear and rotary tables, thruster and a possible configuration of diagnostic tools.

measurements can be performed. The current setup requires a minimum chamber diameter of about 2 m and a minimum chamber length of about 2.5 m.

At present, the AEPD platform can be equipped with diagnostic tools for beam characterization (Faraday probe, retarding potential analyzer, ExB probe, active thermal probe), optical inspection (telemicroscope, triangular laser head) and thermal characterization (pyrometer, thermo-camera). Table 1 lists the available diagnostic tools with their measurement principle and possible applications. The main performance parameters of the diagnostic tools are summarized in Table 2. In the following, the diagnostic tools including their design are described in more detail.

2.2 Faraday probe

The Faraday probe has been developed in-house [16]. It uses a graphite ion collector rod, which is embedded in a ceramic tube surrounded by a thin metal cylinder of stainless steel with a length of 101 mm and an outer diameter of 6 mm. The ion collecting diameter is as small as 1.9 mm (area 2.8 mm²) to allow for measurements with high spatial resolution. The ion collector is connected via a shielded BNC cable and a customized vacuum feedthrough to an external board with several high-precision resistors with different resistance. Thus, a large range of signal amplitudes can be covered. Data are recorded using a 12-bit analogue digital converter. With a sampling rate of up to 20 kHz, maximum ion current densities up to 40 mA/cm² with a resolution of 0.05 mA/cm² can be detected.

The Faraday probe is designed as small and compact as possible in order to minimize the interaction with the energetic particle beam. Thus, this probe can also be used to measure the ion current density at a very low distance to the thruster exit plane, which gives access to determining the plasma density inside the discharge chamber.

Table 1. List of diagnostic tools with operation principle and possible measurement applications.

Diagnostic tool	Specifications
Faraday probe	Current density measurements Beam profiling
Retarding potential analyzer	Electrostatic energy analyzer Energy distribution measurements of charged particles
ExB probe	Ion velocity filter Velocity distribution measurements of charged particles Ion species fractions composition
Active thermal probe	Energy flux density measurements Measurement of energy flux density distribution
Telemicroscope	Detection of divergence and irregularities in the beam profile High-resolution optical imaging
Triangular laser head	Inspection and radial erosion measurements of mechanical parts Distance measurements using the triangulation principal
Pyrometer	Surface profiling and axial erosion measurements of mechanical parts Spot measurement of emitted infrared radiation
Thermocamera	Surface temperature measurements of mechanical parts Imaged measurement of emitted infrared radiation Surface temperature images of mechanical parts

The potential of the measuring area is defined by the potential drop at a resistor, whose resistance is, typically, selected such that the potential drop is smaller than 1 V, i.e. it is negligibly small with respect to the beam voltage. The direct calibration of the Faraday probe is not possible because there is no ion current standard. Therefore, the Faraday probe calibration is performed by precisely measuring the resistance and probe area.

2.3 Retarding potential analyzer

The retarding potential analyzer was also developed in-house with the goal to make it as small as possible while keeping the performance (signal-to-noise ratio) sufficiently high. Therefore, a two-grid design with 149 holes has been chosen. The device consists of two grids and an ion collector. The first grid is used for focusing the ion trajectories, the second grid for repelling secondary electrons. The ion collector is used for measuring the ion current and for repelling the ions by applying a repelling voltage U_r . The holes of the first grid have a diameter of 0.4 mm. The first grid could also be used for measuring the ion current density. The measurement area is $24 \times 24 \text{ mm}^2$. The ion collector has cup-shaped cavities, one for each of the 149 ion channels. The repelling voltage can be varied between 0 V and 3000 V with an accuracy better than 0.05%. The collected ion current is transformed by a high-precision resistor into a voltage drop, which is measured by a 14-bit AD converter.

The diameter of the grid holes is chosen such that it is close to the Debye length λ_D . The Debye length of a plasma can be calculated by the following equation:

$$\lambda_D = \sqrt{\frac{\epsilon_0 k T_e}{n_e e^2}} \quad (1)$$

and the continuum equation:

$$j = q_0 n_e v \quad (2)$$

ϵ_0 , k , T_e , n_e , and e are vacuum permittivity, Boltzmann constant, electron temperature, electron density, and elementary charge, respectively. j , q_0 and v are current density, charge and velocity of the ions. Hence, the Debye length depends on current density and ion velocity (or ion energy). In the regime of interest, i.e. for current densities between 1 mA/cm^2 and 10 mA/cm^2 , and ion energies between 100 eV and 2000 eV, the Debye length varies between 0.2 mm and 0.6 mm.

The retarding potential analyzer measures the current I_c at the collector as a function of the repelling voltage U_r . The energy distribution $f(E)$ is then calculated by:

$$f(E) \propto -\frac{dI_c}{dU_r} \quad (3)$$

The maximum of the energy distribution would be a measure for the ion current density. However, quantifying the current density using the current at the collector is impossible, because the transmission of the ions through the grids must not be 100%. Therefore, the energy distribution is normalized to its maximum.

The ion energy distribution is measured with respect to the ground of the vacuum chamber. The ground of the ion thruster and its components is not connected to the vacuum chamber ground. The difference is called secondary star ground (SSG) potential. The SSG potential is negative with respect to the ground of the vacuum chamber and depends on the operation conditions of the thruster.

2.4 ExB probe

The ExB probe exploits the action of a magnetic (B) and an electric field (E) to select ions on the basis of their velocity v_i : only ions whose velocity satisfies the Wien condition (Eq. (4)) are able to pass through the filter and thus being detected [17]. d is the distance between the fixed

Table 2. Summary of selected specifications and performance parameters of the diagnostic tools.

Diagnostic tool	Parameters
Faraday probe	Sensor area diameter: 1.9 mm Measurement range: up to 40 mA/cm ² Accuracy: <0.01 mA/cm ² (depends on dynamic range)
Retarding potential analyzer	Outer dimension: 101 mm (length), 6 mm (diameter) Number / diameter of holes: 149 / 1.8 mm Measurement range: 0 eV–3000 eV Accuracy: <5 eV
ExB probe	Dimension (including housing): 40 × 47 × 84 mm ³ Entrance orifice diameter: 1.6 mm Entrance collimator length: 90 mm Wien filter length: 150 mm Resolution: 1000 m/s Velocity range: up to 100 000 m/s
Active thermal probe	Dimension: 50 × 50 × 280 mm ³ Measurement range: 1 × 10 ⁻³ W/cm ² –4 W/cm ² Sensitivity: ±1 × 10 ⁻³ W/cm ²
Telemicroscope	Sensor dimension: 7 × 10 × 0.3 mm ³ Focal length / extension tube length*: 50 mm/40 mm Image size/working distance: 8.75 × 6.56 mm ² /112.5 mm Resolution*: 1600 × 1200 pixel Radial accuracy: <0.01 mm Depth of field: ±0.5 mm
Triangular laser head	Dimension (including housing): 60 × 70 × 210 mm ³ Spot size*: <0.2 mm (at a working distance of 150 mm) Distance range*: 110 mm–190 mm Repeatability*: <0.001 mm Distance resolution: <0.01 mm
Pyrometer	Dimension (including housing): 95 × 47 × 127 mm ³ Spectral range*: 2.3 μm Spot size*: 1.5 mm (at the focal distance of 110 mm) Temperature range/resolution*: 150 °C–1000 °C/0.1 °C System accuracy*: 0.3% of reading +2 °C Repeatability*: 0.1% of reading +1 °C
Thermocamera	Dimension (including housing): 25 × 30 × 47 mm ³ Spectral range*: 7.5 μm–13 μm Image size*: ~0.05 m × 0.07 m (at a distance of 500 mm) Resolution*: 160 × 120 pixel Lateral resolution*: 1.5 mm (at a distance of 500 mm) Temperature range/resolution*: 0 °C–900 °C/0.1 °C System accuracy*: 2% of reading or 2 °C Dimension (including housing): 56 × 60 × 143 mm ³

*Numbers specified by the manufacturer.

electrodes, where the electric field is created:

$$v_i = \frac{E}{B} = \frac{V_{\text{probe}}}{Bd}. \quad (4)$$

Because the velocity is a function of charge state z_i , mass m_i and ion energy $E_{\text{ion},i}$, different ion species can be separated. Equation (5) expresses the electrodes voltage difference associated with each peak in the spectrum: On one hand a constant magnetic field is used to deflect trajectories of the ions, on the other hand a variable electric field acts for compensating the magnetic force, which allows ions with different velocity to be detected as a function of the voltage applied to electrodes. The retarding potential analyzer measures the current I_c at the collector

in dependence on a repelling voltage U_r , which gives direct access to the energy distribution of energetic ions. In contrast to that, the voltage range to be scanned with the ExB probe depends also on the constructive parameters of the probe (magnetic field intensity, electrodes separation). These constructive parameters affect the performances of the probe in terms of resolution. The probe detector is simply constituted by the collector of a Faraday cup:

$$V_{\text{probe}} = Bd \sqrt{\frac{2z_i E_{\text{ion},i}}{m_i}}. \quad (5)$$

The main aim was to develop a probe, which is able to put together high performances with low invasiveness. These aspects can be considered conflicting because an increase

of the probe resolution can be determined by an increase of the magnetic field, and an increase of the magnetic field is usually associated with larger magnets. This problem was overcome by exploiting a particular magnetic configuration known as Stelter dipole [18] allowing a significant increase of the magnetic field with respect to a traditional dipole with the same overall dimension. In particular, a maximum field of 0.54 T has been obtained for a probe having a $50 \times 50 \text{ mm}^2$ section.

Another important aspect taken into account in the probe design concerns the topology of the magnetic and electric fields at the entrance and the exit of the probe. The different decaying behavior of the fields makes the probe not ideal, thus the Wien condition is no more satisfied in these regions. To overcome this problem the electrodes shape has been optimized in order to make the electric fringing field matching the magnetic one. The spatial resolution of the probe is determined by two collimators at the entrance and exit of the probe selecting ions traveling along a well-defined direction. A modular design approach has been implemented allowing to easily change the collimator length and the orifice diameter.

The probe is mainly used to determine the plasma composition in terms of ion species fraction because of the dependence of the ion velocity on the charge state. Assuming that all ion species are subject to the same accelerating voltage, the separation between the peaks position will be given by $\sqrt{z_i/m_i}$. The area under each peak yields the current carried by each ion species. Therefore, the ratio between this area and the area under the overall spectrum provides the current fraction (neglecting secondary emission effects). On the other hand the position of each peak is connected with the ion velocity through the constructive parameters of the probe: in particular the ion velocity distribution function for each ion species could be determined. This application requires a calibration of the probe providing a correction factor to be applied to the measured ion velocity to obtain the real one.

2.5 Active thermal probe

The active thermal probe (see Fig. 2) was developed as a flexible diagnostic for the measurement of energy flux. For the use as a diagnostic tool for beam characterization as a part of the AEPD platform, it has been further improved and characterized especially regarding its sensitivity towards parasite heat sources.

The physical principle of the measurement method of the active thermal probe is based on the compensation of the incoming energy by decreasing the heating power of a preheated probe. The probe consists of a ceramic dummy-substrate (see Fig. 2a), which is electrically heated to a given set-point temperature. If the probe is exposed to an external energy flux (e.g. by the ion beam) the additional heating of the probe is compensated by a reduction of the electrical heating power, resulting in a constant temperature of the probe. The power of the external energy source is then directly given by the difference in the electrical heating power. In contrast to the other probes, the ATP

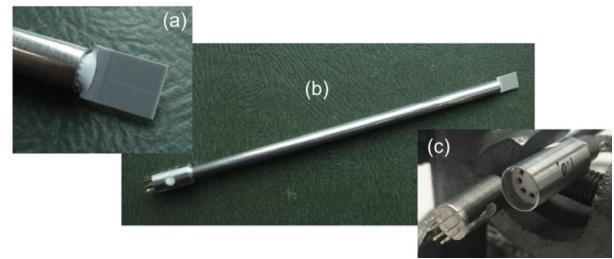


Fig. 2. Active thermal probe: sensor area (a), full image (b) and connector (c).

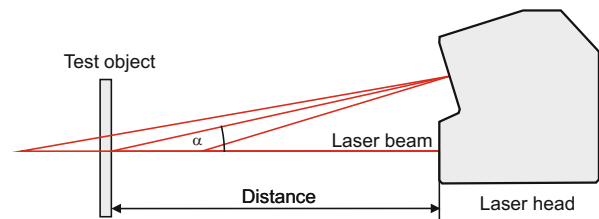


Fig. 3. Measurement principle of the triangular laser head (triangulation effect).

measures both the contribution of charged and neutral particles. A much more detailed description of the working principle of the active thermal probe can be found in references [19–21].

2.6 Telemicroscope and triangular laser head

The telemicroscope is a high-resolution optical camera, which can be used to measure radial (and axial) erosion of mechanical parts. It consists of a CCD camera, an extension tube and a photographic lens. By placing the extension tube between camera and lens, the radial resolution and depth of field is reduced considerably (lateral resolution from formerly 0.15 mm to 0.01 mm; depth of field from formerly 60 mm to 0.5 mm).

The triangular laser head measures the distance to a test object utilizing the triangulation principle, i.e. the fact that the detection angle α depends on the distance between triangular laser head and test object (see Fig. 3). When scanning across the test object, the surface profile can be measured, which gives access to axial (and radial) erosion.

Telemicroscope (The Imaging Source DFK 51AU02) and triangular laser head (Keyence LK-G152) are commercial devices. The triangular laser head is the same one that was used with the previous setup [12]. The telemicroscope has changed slightly with the goal to reduce the overall dimension. Now a smaller lens and a camera with a higher resolution is used. Triangular laser head and telemicroscope are operated inside vacuum. Therefore, some vacuum-sensitive electronic parts (capacitors) had to be replaced. For safety reasons the devices are covered by a small housing each. The overall dimensions could be reduced considerably compared to the previous setup



Fig. 4. Telemicroscope with housing (without metal cover).

with vacuum-sealed housings [12]. The new housings consist of a metal base plate, a front plate made of graphite with sapphire window(s) and a metal cover. The window protects the optics from direct particle impingement. Additionally, the telemicroscope housing is equipped with four high-power LEDs for illumination. Figure 4 shows, exemplary, the housing of the telemicroscope.

2.7 Pyrometer and thermocamera

Pyrometer and thermocamera measure the surface temperature of a test object upon detection of the emitted infrared radiation. The physical principles are described by Planck's law:

$$B(T, \varepsilon, \lambda) = \varepsilon t \frac{2hc^2}{\lambda^5} \frac{1}{\exp\left(\frac{hc}{\lambda kT}\right) - 1} \quad (6)$$

i.e. the intensity of the emitted infrared radiation B depends on the object temperature T , the emissivity ε of the object material, the wavelength λ and, if needed, the transmission t of a window between test object and pyrometer/thermocamera. h , c and k are Planck constant, speed of light and Boltzmann constant, respectively.

When measuring the temperature, the properties of the test object, i.e. the emissivity of the material of interest, and of the setup, i.e. window effects, must be known. Emissivity (graphite of grid area: $\varepsilon = 0.97$) and transmission of the windows (sapphire window for pyrometer: $t = 0.85$; ZnS window for thermocamera: $t = 0.75$) were measured in the spectral region of interest.

Pyrometer (Optris CT 3M) and thermocamera (Optris PI) are commercial devices. Unlike the previous setup [10,12], which contained only a pyrometer, the actual platform uses a pyrometer of different type and additionally a thermocamera. Both devices were chosen because of their small size, which reduces possible interactions with the energetic particle beam. Pyrometer and thermocamera are operated inside vacuum. Therefore, some vacuum-sensitive electronic parts (capacitors) had to be replaced or removed (liquid crystal display). Both diagnostic heads



Fig. 5. Pyrometer sensor head with housing.

Table 3. Summary of operation parameters of the RIT- μ X at operation point 1 (OP1) and 2 (OP2).

Parameter	OP1	OP2
Beam Voltage	1050 V	1700 V
Beam Current	4 mA	8 mA
Accelerator voltage	-200 V	-250 V
Nominal thrust	210 μ N	540 μ N

are placed inside metal housings with appropriate windows (pyrometer: sapphire window; thermocamera: ZnS window) for safety reasons [14]. The housing of the pyrometer is shown in Figure 5, the housing of the thermocamera is similar to that of the telemicroscope in Figure 4.

Operating the diagnostic heads inside vacuum has the advantage that they can be brought closer to the test object. A smaller working distance results in a better lateral resolution, which is especially favorable for the thermocamera.

2.8 Thruster

A gridded ion thruster RIT- μ X [15] was used for the test measurements. Radio-frequency ion thrusters (RITs) generate thrust in two steps: in the first step the propellant is ionized in the oscillating electromagnetic field of a coil (plasma). Once ionized, the propellant is accelerated in the electrostatic field of the thruster's second functional unit called the grid system.

The ionization chamber of the RIT- μ X has an inner diameter of 4 cm at the interface to the grid system and a length of 3 cm. Its inductively coupled plasma is operated with a frequency of 2.5 MHz. The experiments were performed using the standard propellant xenon. The RIT- μ X can be equipped with different sets of grids optimized for specific mission requirements. During the reported tests a configuration with 37 extraction channels was used. It is designed for extraction voltages in the range from 600 V to 2200 V and nominal ion currents between 1 mA and 10 mA. The thruster was operated here at two operation points as summarized in Table 3.

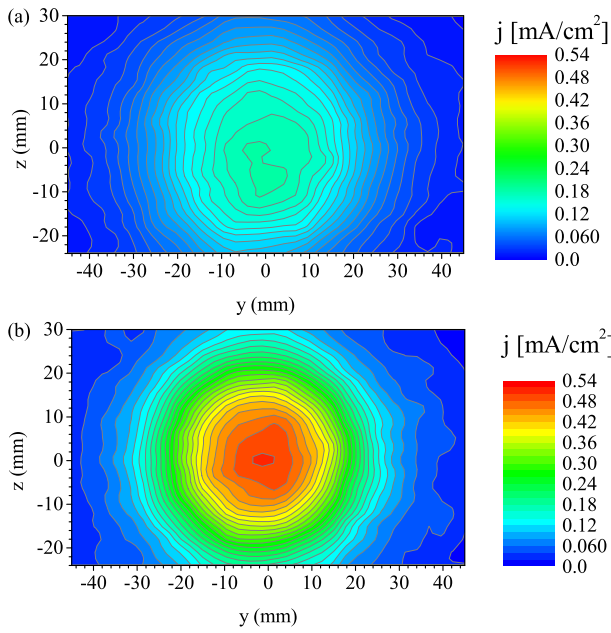


Fig. 6. Current density maps of the RIT- μ X at OP1 (a) and OP2 (b) measured with the Faraday probe at a distance of 120 mm to the exit plane of the thruster.

2.9 Test chamber

The tests were performed in the Jumbo test facility [22]. The tank is of cylindrical shape with a diameter of 2.6 m, a length of 6 m and a volume of 30 m³. It is equipped with turbo and cryo pumps with a total pumping speed of 120 000 L/s for nitrogen or 65.000 L/s for xenon. The base pressure is about 1×10^{-7} mbar.

3 Results

3.1 Faraday probe

Selected current density maps of the thruster at the two operation points are plotted in Figure 6. As expected, rotationally symmetric, Gaussian shaped beam profiles can be seen with a higher maximum current density at operation point 2 ($j_{\max} = 0.52$ mA/cm²) than at operation point 1 ($j_{\max} = 0.18$ mA/cm²). This is related to the higher beam voltage at operation point 2. The full width at half maximum of the beam profiles is 48.0 mm for OP1 and 40.8 mm for OP2.

3.2 Retarding potential analyzer

Measurements with the retarding potential analyzer were performed for both operation points, too. Figure 7 shows the measured current curves and the calculated, normalized energy distributions. Both curves are corrected for the SSG potential U_{SSG} . The energy distributions reveal a single peak with a position slightly higher than the corresponding beam voltage (1078 V for OP1; 1716 V for OP2).

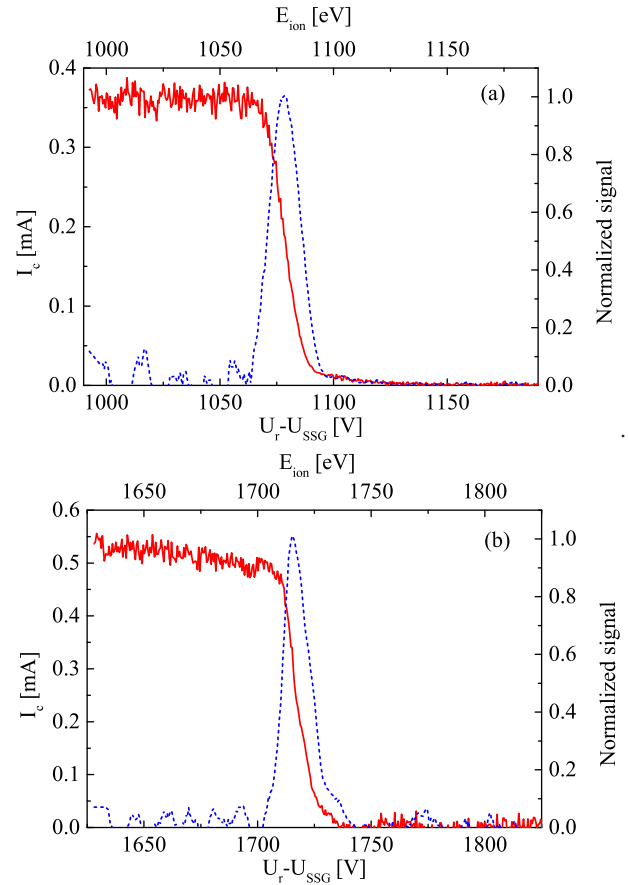


Fig. 7. Current I_c measured with the retarding potential analyzer at the collector (red solid lines) and calculated energy distribution (blue dashed lines) at OP1 (a) and OP2 (b). The curves are corrected for the secondary star ground potential ($U_{SSG} = -42$ V for OP1; $U_{SSG} = -78$ V for OP2).

The difference is related to the plasma potential inside the discharge chamber of the thruster. The full width at half maximum of the peaks is about 16 V for both operation points, which corresponds to less than 2% of the ion energy. Ions with other energies, which could be generated by charge exchange processes, or multiply charged ions were not detected.

3.3 ExB probe

Ion velocity measurements were performed with the ExB probe positioned along the thruster axis at a distance of 350 mm from the thruster exit plane. Figure 8 shows two curves obtained for the two operation points of the thruster. The position of the peaks corresponds to the different ion velocity, which is proportional to the square root of the ion energy. The most pronounced peaks at an electrode voltage difference of ~ 87 eV (OP1) and ~ 111 eV (OP2) can be assigned to singly charged ions (Xe⁺). As expected, the ratio of the peak positions is the same as the square root of the ratio of the corresponding ion energies measured with the retarding potential analyzer.

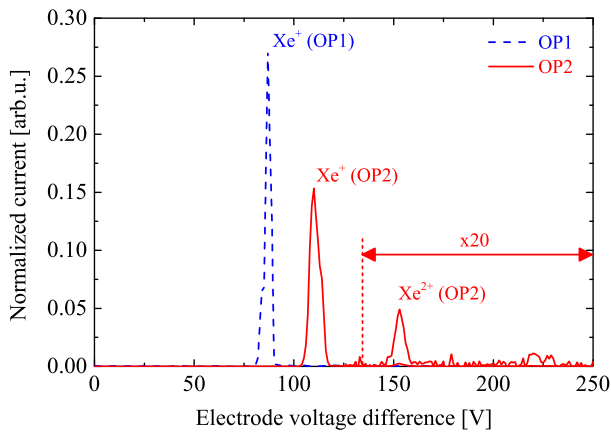


Fig. 8. ExB probe normalized spectra at OP1 (dashed curve) and OP2 (solid curve) at a distance of 350 mm to the exit plane of the thruster.

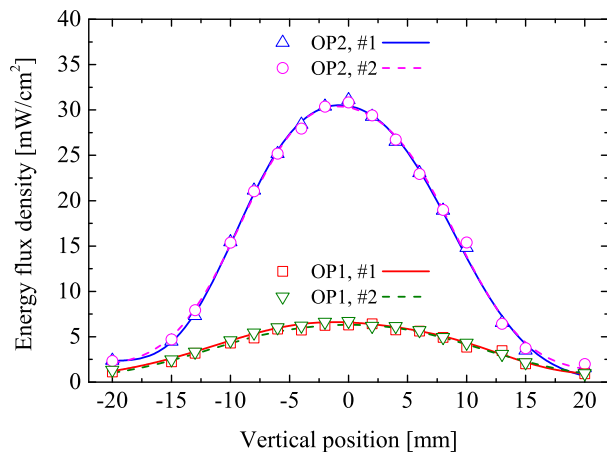


Fig. 9. Energy flux density vs. vertical position for the RIT- μ X running at OP1 and OP2 measured with the active thermal probe. The symbols represent the experimental data, the solid lines give cubic spline interpolations as a guide to the eye. There are two measurements for each operation point.

In the curve for operation point 2 a second peak at an electrode difference voltage of ~ 153 eV can be seen. This peak is related to doubly charged ions (Xe^{2+}). The peak is very small, i.e. the fraction of doubly charged ions is low, as it is typical for gridded ion thrusters.

3.4 Active thermal probe

In Figure 9 selected results for the measurement of the energy flux density under variation of the vertical position relative to the center axis of the thruster are presented. The thruster was aligned in such a way that the beam hits the probe at normal incidence and that the center of the thruster grid has a distance of 490 mm to the probe. Figure 9 summarizes the results of two measurements for the two thruster operation points each. The data illustrate clearly that the measurements show a good reproducibility and give access to the radial distribution of the energy flux density of the beam. Furthermore, it should be pointed out

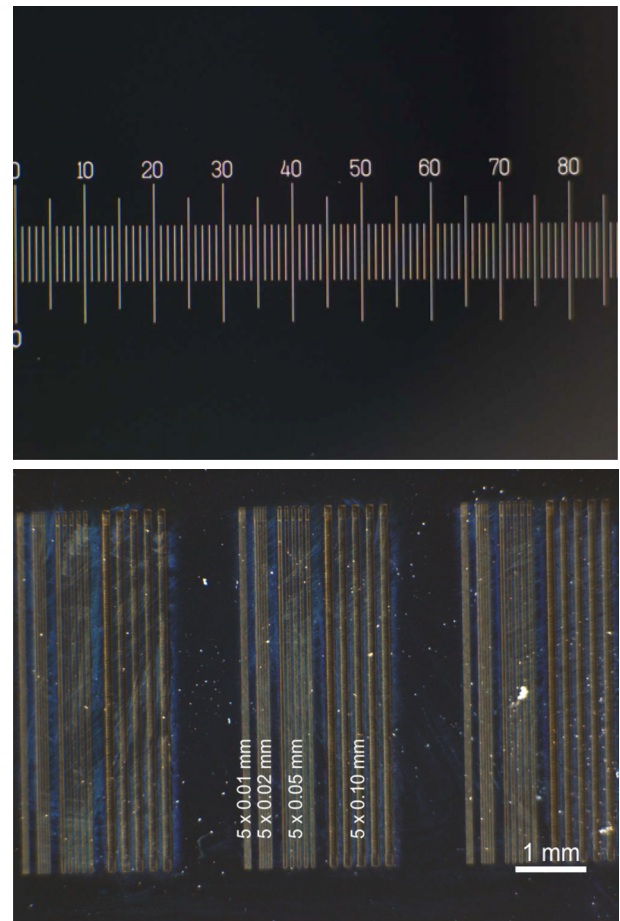


Fig. 10. Telemicroscope image of the test structures: eyepiece graticule (top) and line structure (bottom).

that even close to its lower detection limit of $1 \text{ mW}/\text{cm}^2$ the probe gives reproducible results.

3.5 Telemicroscope

The performance of the telemicroscope was investigated using two test structures: a graticule structure and a special line structure. Both test structures are shown in Figure 10. Using the scale of the graticule structure, the field of view can be easily measured. It was found that the field of view is $8.75 \times 6.56 \text{ mm}^2$ at a working distance of 112.5 mm, and the depth of field is smaller than $\pm 0.5 \text{ mm}$. The line structure consists of several pairs of lines, which were laser scribed into a titanium dioxide layer (dark area) on a silicon wafer. Each pair consists of five lines with equal width and spacing of 0.01 mm, 0.02 mm, 0.05 mm or 0.1 mm. It can be seen in Figure 10 that all pairs of lines down to 0.01 mm can be resolved. Hence the lateral resolution of the telemicroscope is better than 0.01 mm. Figure 11 depicts a section of the grid of the thruster (thruster is off). The grid holes can be clearly resolved and grid hole diameter and, hence, the grid hole erosion are accessible. The diameter of the center hole in Figure 11 is $(1.27 \pm 0.02) \text{ mm}$.

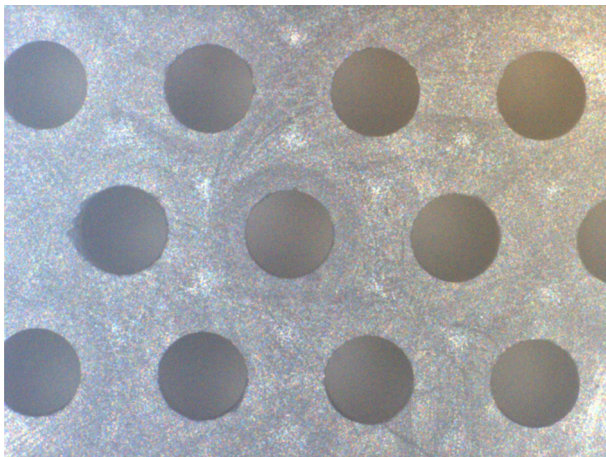


Fig. 11. Telemicroscope image of grid holes of the RIT-μX.

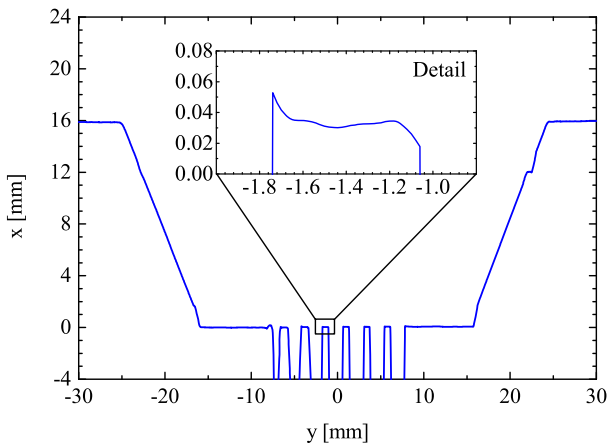


Fig. 12. Surface profile scan across the center of the RIT-μX measured with the triangular laser head. The detail inset shows the measured surface profile scan between two grid holes. The rise of the profile at the left side is a measurement artifact due to the triangulation measurement principle.

3.6 Triangular laser head

Figure 12 shows a surface profile scan of the thruster. Among others, the grid hole area can be identified clearly and the number of holes can be seen. Doing so, the principal shape of the grid including, for instance, its radius of curvature could be measured [7,10]. In case of the RIT-μX the grid is flat. However, there are experimental limitations due to the measurement principle (triangulation effect). Because of that, the triangular laser head might fail in measuring the profile at steep or abrupt edges (see detail inset in Fig. 12).

3.7 Thermocamera

Figure 13 shows thermocamera images of the RIT-μX operated at OP2 and OP1. The surface temperature of almost the whole thruster was imaged. The temperature distribution is nearly homogeneous, apart from the holes. As shown in previous tests, the temperature of the plasma

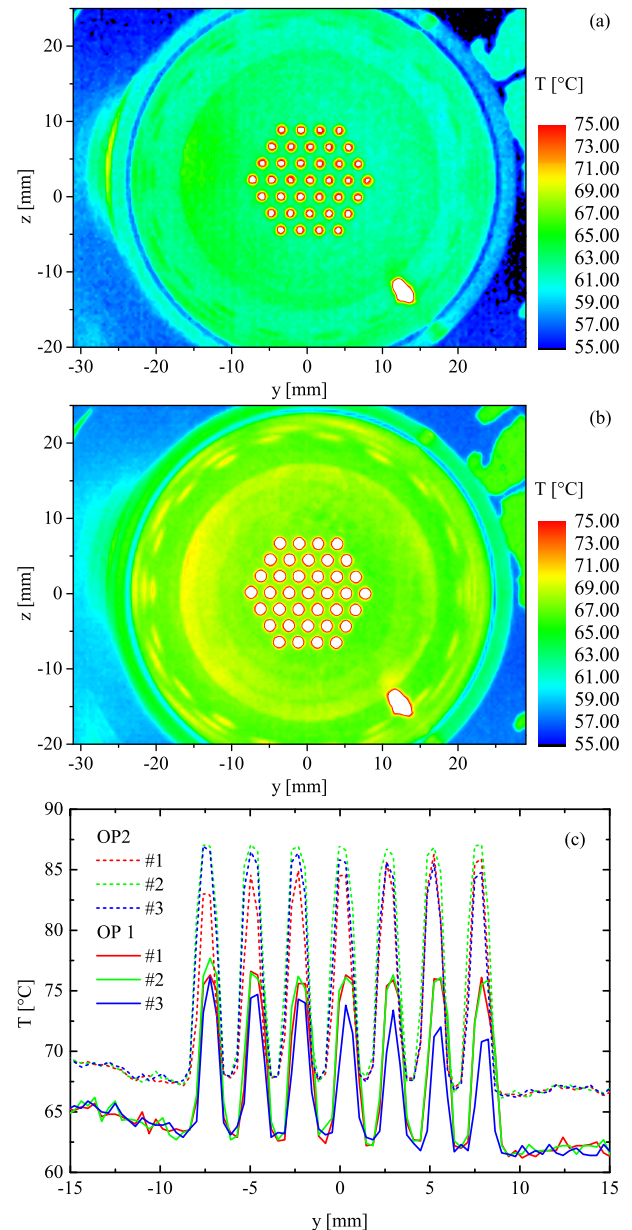


Fig. 13. Thermocamera image of the RIT-μX at OP1 (a) and OP2 (b). (c) Horizontal temperature scans across the center of the thruster extracted from thermocamera images. Please note, the assumed emissivity is that of graphite ($\epsilon = 0.97$). Therefore, the given temperature values are only correct for the grid area.

chamber, which is imaged through the holes is considerably higher than the grid surface temperature [7,10]. In Figure 13c selected temperature line scans for both operation points, which were extracted from thermocamera images, are plotted. There are some interference-like structures. These structures are related to the fact that the sensor pixels of the thermocamera see different fractions of the grid and of the holes. Please note, the height of the maxima differs for the different line scans at the same operation point, whereas the minima and the region on the left and on the right side are the same. Again this is related

to the different fractions of grid and holes seen by the sensor pixels, because the line scans were taken for different z -positions. The grid temperature was found to be $68\text{ °C} \pm 2\text{ °C}$ for OP2 and $63\text{ °C} \pm 2\text{ °C}$ OP1.

No pyrometer data are shown here, because the temperature of all thruster parts is below the lower limit of the measurement range of the pyrometer of 150 °C (see Tab. 2).

4 Conclusion

The experimental data demonstrate impressively the capabilities of the AEPD platform, which allows, for the first time, for a comprehensive in-situ characterization of electric propulsion thrusters or ion beam sources for material processing. Comprehensive characterization is an essential part in the development and optimization process of these devices, and allows to judge the performance with respect to the specific mission or application needs. Furthermore, a standardization of these diagnostics would allow for a reliable comparison of the performance of EP thrusters of different type, which would help promoting EP thruster technologies.

Typically, the main focus lies on investigating beam properties, because the beam provides the thrust or, in material science, the tool for material modification. Important parameters are particle energy or velocity, beam shape and divergence, composition, charge state. All of these parameters can be measured with the current setup. It is not only possible to measure the properties of charged particles (Faraday probe, retarding potential analyzer, ExB probe) but also of energetic neutrals (active thermal probe).

The optical inspection tools (triangular laser head, telemicroscope) provide important information about the shape of mechanical parts and its evolution in time (erosion), which can be life-limiting factors. The triangular laser head is advantageous when measuring axial dimensions, whereas the telemicroscope has its advantage when measuring radial dimensions. However, both devices can be used to measure axial and radial dimensions, though with different accuracy.

Thermal characterization is important, for instance, for evaluating the thermal impact on the performance of satellites (in case of electric propulsion thrusters). Both pyrometer and thermocamera provide similar information. In case of small thrusters, the thermocamera can yield a full thermal image. In case of larger thrusters (with higher power), scanning with the pyrometer seems to be more appropriate because (i) of its smaller dimension and (ii) the smaller time that is needed to perform a line scan instead of taking a thermocamera image.

5 Summary and outlook

We have reported about improvements of our AEPD platform. The activities are focused on modifying the experimental setup in order to reduce possible interactions

between diagnostics and thruster, on implementing additional or alternative diagnostic heads in order to improve the performance or to expand the portfolio of accessible parameters. We have described the main parameters of the new diagnostic tools and presented first experimental results, exemplarily, with a gridded ion thruster RIT- μ X.

It can be stated that the improvements on the AEPD platform have improved reliability and repeatability, and, therefore, constitute a major step towards standardization, which is intended to be the final goal. In order to reach this goal, significant effort is still necessary to provide suitable standards.

Author contribution statement

All authors contributed equally to the paper.

The work was performed with financial support provided by ESA/ESTEC (Contract No. 4000107451/12/NL/RA; “Qualification of the AEPD System as a Standard On-Ground Tool for Electric Propulsion Thrusters”). The authors thank R. Woyciechowski, M. Müller, S. Daum (all Leibniz-Institute of Surface Modification), R. Kukies (Airbus Defence & Space), W. Gärtner, U. Bachmann (all Justus-Liebig-Universität Gießen) for technical support.

References

1. J.P. Verboncoeur, A.B. Langdon, N.T. Gladd, *Comput. Phys. Commun.* **87**, 199 (1995)
2. R. Becker, W.B. Herrmannsfeldt, *Rev. Sci. Instrum.* **63**, 2756 (1992)
3. M. Tartz, E. Hartmann, H. Neumann, *Rev. Sci. Instrum.* **79**, 02B905 (2008)
4. M. Crofton, R. Ueunten, L. Harris, E. Yohnsee, R. Cohen, in *Proceedings of the 32nd AIAA Joint Propulsion Conference and Exhibit, Lake Buena Vista, 1996*, Paper AIAA-96-2977
5. S. Mazouffre, P. Echegut, M. Dudeck, *Plasma Sources Sci. Technol.* **16**, 13 (2007)
6. S. Mazouffre, K. Dannenmayer, J. Pérez-Luna, *J. Appl. Phys.* **102**, 023304 (2007)
7. C. Bundesmann, M. Tartz, F. Scholze, H. Neumann, H.J. Leiter, F. Scortecci, D. Feili, P.E. Frigot, J. Gonzalez del Amo, in *Proceedings of the 31st International Electric Propulsion Conference, Ann Arbor, 2009*, Paper IEPC-2009-160
8. C. Bundesmann, M. Tartz, F. Scholze, H. Neumann, F. Scortecci, S. Scaranzin, P.E. Frigot, J. Gonzalez del Amo, R.Y. Gnizdor, in *Proceedings of the 31st International Electric Propulsion Conference, Ann Arbor, 2009*, Paper IEPC-2009-141
9. T. Misuri, A. Milani, M. Andrenucci, in *Proceedings of the 31st International Electric Propulsion Conference, Ann Arbor, 2009*, Paper IEPC-2009-036
10. C. Bundesmann, M. Tartz, F. Scholze, H. Neumann, H.J. Leiter, F. Scortecci, *J. Propul. Power* **27**, 532 (2011)

11. T. Misuri, T. Vrebosch, L. Pieri, M. Andrenucci, M. Tordi, E. Marcuzzi, M. Batolozzi, S. Renzetti, J. Gonzalez del Amo, in *Proceedings of the 32nd International Electric Propulsion Conference, Wiesbaden, 2011*, Paper IEPC-2011-129
12. C. Bundesmann, M. Tartz, F. Scholze, H.J. Leiter, F. Scortecci, R.Y. Gnizdor, H. Neumann, *Rev. Sci. Instrum.* **81**, 046106 (2010)
13. D. Pagano, F. Scortecci, C. Bundesmann, C. Eichhorn, F. Scholze, H. Neumann, H. Leiter, H. Kersten, S. Gauter, R. Wiese, R. Blott, P.J. Klar, K. Holste, B. Meyer, S. Mazouffre, A. Bulit, J. Gonzales del Amo, in *Proceedings of the 34th International Electric Propulsion Conference, Hyogo-Kobe, 2015*, Paper IEPC-2015-363
14. C. Bundesmann, C. Eichhorn, F. Scholze, H. Neumann, H.J. Leiter, F. Scortecci, in *Proceedings of the 34th International Electric Propulsion Conference, Hyogo-Kobe, 2015*, Paper IEPC-2015-392
15. C. Altmann, H. Leiter, R. Kukies, in *Proceedings of the 34th International Electric Propulsion Conference, Hyogo-Kobe, 2015*, Paper IEPC-2015-274
16. C. Eichhorn, F. Scholze, C. Bundesmann, H. Neumann, in *Proceedings of the 33rd International Electric Propulsion Conference, Washington, 2013*, Paper IEPC-2013-295
17. D. Renaud, D. Gerst, S. Mazouffre, A. Aanesland, *Rev. Sci. Instrum.* **86**, 123507 (2015)
18. K. Halbach, *Nucl. Instrum. Methods* **169**, 1 (1980)
19. R. Wiese, Dissertation, Ernst-Moritz-Arndt Universität, Greifswald, 2008
20. R. Wiese, H. Kersten, G. Wiese, M. Häckel, *Vakuum in Forschung und Praxis* **23**, 20 (2011)
21. R. Wiese, H. Kersten, G. Wiese, R. Bartsch, *Eur. Phys. J. Techniques and Instrumentation* **2**, 2 (2015)
22. P.J. Klar, K. Hannemann, U. Ricklefs, H. Leiter, in *Proceedings of the 34th International Electric Propulsion Conference, Hyogo-Kobe, 2015*, Paper IEPC-2015-89